

SIMULATION OF THE SOUND RADIATION OF TURBULENT FLOWS WITH DES

**U. Michel*, D. Eschricht, B. Greschner, T. Knacke,
C. Mockett, L. Panek, F. Thiele, and J. Yan****

*Institute of Fluid Mechanics and Engineering Acoustics, Berlin University of Technology
Müller-Breslau-Str. 11, 10623 Berlin
Email: ulf.michel@cfd.tu-berlin.de*

**) also with DLR, Institute of Propulsion Technology, Engine Acoustics, Berlin
**) now with Voith Siemens Hydro Power Generation GmbH & Co. KG,
Corporate Technology – R&D
Alexanderstrasse 11, 89510 Heidenheim, Germany*

Key words: noise emission, numerical simulation, detached eddy simulation, DES, computational fluid dynamics, CFD, computational aeroacoustics, CAA, jet mixing noise, airframe noise, slat noise, trailing edge noise, interaction noise.

Abstract. Detached eddy simulation (DES) is a suitable method for the simulation of the sound radiation of turbulent flows, providing access to resolved turbulent scales at minimal computational cost. The near-wall region is solved efficiently by RANS while LES is applied to detached regions of large scale turbulence. The various DES implementations of the Institute of Fluid Mechanics and Engineering Acoustics (ISTA) at the TU-Berlin are described. Simplified academic flow cases are used for the validation of the method and the suitability of the method for complex industrial flow applications is also demonstrated. The method proves robust and reliable for a wide range of applications, ranging from external to internal flows, from bluff bodies with massive separation to the partial resolution of attached boundary layers. Examples of applications to noise emission problems are presented for (i) slat noise, (ii) interaction noise, (iii) jet mixing noise, and (iv) trailing-edge noise. The jet noise predictions include a study on the influence of serrations on the noise emission. The overall sound pressure levels as well as the noise reducing effect of the serrations are well predicted. With respect to the prediction of flow noise, further work is required to improve the predictive capabilities for higher frequencies.

1 INTRODUCTION

The reduction of noise emission has been a significant concern in the design of new aircraft over the last five decades. In this process the emitted sound power per unit thrust was reduced by about 99.5% (23 dB) when compared to the first jet powered transport aircraft. Due to the persistent growth of air traffic, this is still not considered sufficient and a further reduction by a factor of five (7 dB) to 99.9% is the goal of the industry until 2020. One can imagine that the objective of reducing the noise emission of comparably quiet aircraft becomes more and more difficult. At the same time the fuel consumption must be reduced, further compounding the task. Noise levels have to be

guaranteed by the airframe and engine manufacturers to customers already in the early design stages. This is currently based on experience from earlier designs, on model tests and, to an increasing degree on to numerical studies. This paper is concerned with the development of improved numerical prediction methods for the sound emission of turbulent flows of direct relevance to the civil aerospace industry.

Aircraft noise consists of both engine and airframe noise. Concerning the engine, traditionally the strongest source during take-off has been jet mixing noise. However, due to the substantial reduction of this over the years, other engine noise sources have become important, an example being fan noise, which propagates upstream through the engine intake and downstream through the bypass duct and radiates into the far-field. The most effective way to reduce jet mixing noise is to reduce the exhaust speed of the engine which requires an increased mass flow rate through the engine to maintain thrust. This was realised by increasing the bypass ratios of the engines up to values between nine and ten on the latest engine designs. These engines are installed in so-called short cowl nacelles, where the nozzle of the bypass duct is shorter than the primary nozzle of the engine (staggered nozzles). This design is lighter than a long-cowl nozzle, which has a common nozzle for both streams, however the short cowl is noisier and it would be a great success if it were possible to verify this numerically and show why this is so.

Unfortunately, the increase of bypass ratios yields heavier engines with larger nacelles, which increase the drag of the aircraft and make it more difficult to install the engines under the wing, which is the best solution with respect to aircraft weight. In recent years, a new technique has been developed that reduces jet mixing noise by a factor of the order of two with respect to sound power (3 dB). This is achieved by adding serrations (chevrons) to the nozzles of the engines. These serrations are directed slightly toward the centre of the nozzle, yielding a pair of longitudinal vortices on each serration. The vortices enhance the mixing in the vicinity of the nozzle and yield a thicker shear layer and a shorter jet with lower turbulence levels. One undesired side effect of the serrations is that the generation of the longitudinal vortices requires power, hence slightly increasing the fuel consumption of the engine. Concerning the noise, it can happen that the reduction of the noise at the peak frequency of jet mixing noise is accompanied by an unwanted noise increase at higher and better audible frequencies. Subtle changes of the design of the serrations determine this effect at higher frequencies. The optimum design is currently developed with the aid of expensive and time consuming model tests. A trustworthy numerical method could speed up the design and reduce the development costs substantially.

A further contribution to aircraft noise is airframe noise, primarily the wind noise of the high lift system and landing gear particularly during the landing approach. One of the major airframe noise sources is that emitted by the slat on the leading edge of the wing. Slats are used on all modern aircraft to ensure that the flow remains attached on the upper surface of the wing at high angles of attack. The slat geometry is optimised with models in extensive aerodynamic wind tunnel tests. The noise emission is experimentally studied with the aid of phased microphone arrays in aeroacoustic wind tunnels. An experimental capability to investigate the noise emission simultaneously with the aerodynamics was added recently in some wind tunnels. But here again, it would be ideal, if the optimum design with respect to the noise emission could be determined using numerical methods.

Detached Eddy Simulation (DES) is one numerical method that promises to offer the required features, and was originally proposed by Spalart et al.³⁴ (1997). The Institute of

Fluid Mechanics and Engineering Acoustics (ISTA) at the TU-Berlin has developed numerous implementations of the DES method. In this development process, much hands-on experience has been gained in a variety of different situations, and it is the aim of this paper to summarise the salient points of this experience.

The paper consists of three parts. The current status of the method at ISTA is described in section 2. Validation exercises based on generic or academic flow cases are discussed in section 3, which includes a discussion of remedies for some problems of the method. The effectiveness of these is demonstrated on a range of industrially-relevant applications in section 4. In the conclusions, remaining open issues and the intended direction of future research are outlined.

2 SIMULATION OF SOUND EMISSION WITH DES

2.1 Source modelling with DES

The Navier-Stokes Equations do not only describe turbulent flows but also their sound radiation. A direct numerical simulation (DNS) of the sound radiation is not possible with available computer resources for the Reynolds numbers of technical interest. Therefore, the problem is solved via a zonal approach. Only the flow region with aerodynamic sources is simulated by solving the Navier-Stokes equations with sufficient precision. The far-field radiation is then computed by solving integrals over a control surface based on acoustic analogies. In certain cases it is useful to define intermediate zones in which the sound propagation is solved with methods provided by Computational Aeroacoustics (CAA). The fan of an aero-engine is an example in which the sound propagation upstream and downstream of the fan stage is computed in such a way (Li et al. ^{13,14}). The sound attenuation of the duct lining must be included (Li et al. ¹⁵, Richter et al. ²⁶) to make this propagation computation technically interesting.

To reduce the computational effort in the source region, the precise DNS is substituted by less expensive methods such as Large Eddy Simulation (LES) or Detached Eddy simulation (DES). Both methods rely on modelling the smaller scales while the larger scales are resolved in space and time. The difference between LES and DES lies in the treatment of the turbulent boundary layers. The resolution requirements of LES in the near wall region lead to unfeasibly fine grids for higher Reynolds number flows. For this reason, the nozzle surface is often excluded entirely from the computational domain in LES of jet flows (Bogey et al. ³) or treated using approximate wall functions (Andersson et al. ^{1,2}).

DES is a hybrid RANS-LES method that applies RANS to the near-wall region and LES to separated flow regions, and is aimed at bridging the gap that exists between conventional RANS and LES methods in terms of computational expense and predictive accuracy. Since its conception (Spalart et al. ³⁴), DES has received a high amount of attention. A particular advantage in comparison to LES is that it is not necessary to introduce small disturbances near the inflow to seed the turbulence and that it is rather easy to model complicated nozzle geometries in jet noise studies.

A number of shortcomings were identified with the original method, some of which are addressed in this paper.

2.2 Equations for turbulent flow prediction

For acoustic source simulations using DES, the governing Reynolds-averaged continuity, momentum and energy equations are solved for the flow field.

$$\frac{\partial \rho}{\partial t} + \frac{\partial(\rho u_i)}{\partial x_i} = 0, \quad (1)$$

$$\frac{\partial(\rho u_i)}{\partial t} + \frac{\partial(\rho u_i u_j)}{\partial x_j} = -\frac{\partial p}{\partial x_i} + \frac{\partial \sigma_{ij}}{\partial x_j} + \frac{\partial \tau_{ij}}{\partial x_j}, \quad (2)$$

$$c_p \left[\frac{\partial(\rho T)}{\partial t} + \frac{\partial(\rho u_i T)}{\partial x_i} \right] = \frac{\partial p}{\partial t} + u_i \frac{\partial p}{\partial x_i} - \frac{\partial \dot{q}_i}{\partial x_i} + (\sigma_{ij} + \tau_{ij}) \frac{\partial u_j}{\partial x_i}, \quad (3)$$

$$p = \rho RT, \quad (4)$$

where σ_{ij} and τ_{ij} are the viscous stress tensor and the turbulent stress tensor, respectively, and c_p is the specific heat capacity for constant pressure. The turbulent stresses correspond to the Reynolds stresses in the case of RANS modelling, or the subgrid-scale stresses in the case of LES. The viscous and turbulent stresses are defined as

$$\sigma_{ij} = 2\mu(S_{ij} - \frac{1}{3}S_{kk}\delta_{ij}), \quad (5)$$

$$\tau_{ij} = 2\mu_t(S_{ij} - \frac{1}{3}S_{kk}\delta_{ij}) - \frac{2}{3}\rho k \delta_{ij}, \quad (6)$$

whereby S_{ij} is the strain rate tensor

$$S_{ij} = \frac{1}{2} \left(\frac{\partial u_i}{\partial x_j} + \frac{\partial u_j}{\partial x_i} \right) \quad (7)$$

and μ_t is the turbulent dynamic viscosity. The heat flux \dot{q}_i appearing in the energy equation is modelled using a temperature gradient approach:

$$\dot{q}_i = c_p \left(\frac{\mu}{Pr} + \frac{\mu_t}{Pr_t} \right) \frac{\partial T}{\partial x_i} \quad (8)$$

where for air $Pr = 0.71$ (up to about 600 K), and $Pr_t = 0.9$.

For many of the validation cases computed without the resolution of acoustic phenomena (presented in Section 3), the approximation of incompressible flow is acceptable and results in significant simplification of the remaining continuity and momentum equations.

The turbulent dynamic viscosity μ_t is provided by the DES model, and DES has been implemented on the basis of a wide variety of RANS models. Rather than to exhaustively list the formulations of these, reference will be made to publications where

the details are presented. Attention will be constrained to the DES implementation methodology common to all models, plus some specific relevant modifications.

The RANS models employed span a wide scale of mathematical complexity, beginning with the one equation Spalart–Allmaras model³³ with Edwards correction⁵ (denoted SAE) and strain-adaptive linear Spalart–Allmaras variant of Rung et al.²⁸ (SALSA). Two-equation models are represented by the Wilcox $k-\omega$ model³⁹ (WCX) and linear local realisable (LLR) $k-\omega$ model of Rung et al.²⁷. The compact explicit algebraic stress model (CEASM) of Lübcke et al.¹⁶ represents the highest level of modelling complexity considered.

The modification of a RANS model for DES requires the identification of the RANS model length scale L_{RANS} , which is the wall normal distance d_w in the case of the one-equation models considered, and a function of the two turbulence parameters (i.e. k and ε or k and ω) for the remaining models. This is then substituted by the compound DES length scale, which consists of a minimum of L_{RANS} and the LES length scale given by $L_{\text{LES}} = C_{\text{DES}}\Delta$:

$$L_{\text{DES}} = \min(L_{\text{RANS}}, C_{\text{DES}}\Delta). \quad (9)$$

The DES therefore operates in either the original RANS mode, or in a modified LES mode achieved by basing the turbulent length scale on the numerical grid size, Δ , multiplied by a model parameter C_{DES} analogous to the well known Smagorinsky LES model. Indeed, a model formulation identical to the Smagorinsky model can be derived from a DES model in LES mode, under the assumption of local equilibrium^{37,42}. The value of C_{DES} is model specific, and is obtained by calibration against decaying isotropic turbulence^{4,8,42}. It is standard practice in DES to define the grid filter length as³⁶

$$\Delta = \max(\Delta_1, \Delta_2, \Delta_3). \quad (10)$$

An alternative definition commonly used in LES is

$$\Delta = (\Delta_1 \Delta_2 \Delta_3)^{1/3}. \quad (11)$$

The subscripts 1, 2, and 3 denote the three coordinate directions defined by a curvilinear grid. The second definition yields much smaller scales in the case of highly stretched grids. Even smaller values of Δ are achieved with the definition

$$\Delta = \min(\Delta_1, \Delta_2, \Delta_3), \quad (12)$$

which was used with great success in the LES of jet mixing noise by Andersson et al.². It must however be noted that such reductions of the Δ definition are highly case-specific modifications targeted at improving performance for the early shear layer of such high Reynolds number jet flows, which cannot be sufficiently resolved due to computational limitations. These modifications are certainly not generally applicable, and to be handled with care. An alternative, and perhaps more elegant approach of applying “implicit” LES, in which no subgrid-scale model is used, has been proposed by Shur et al.^{31,32} also with considerable success.

In addition to the standard substitution of the DES length scale in the destruction term of the model k equation only, it was proposed by Yan et al.⁴² to introduce the length scale L_{DES} also into the turbulence eddy viscosity expression of the Wilcox $k-\omega$ model,

$$\mu_t = \rho c_\mu L_{\text{DES}} k^{1/2}. \quad (13)$$

It was shown by Yan et al.⁴³ that this approach yields superior results for the prediction of jet mixing noise.

- As a result of numerous studies of the original DES method, several key shortcomings were identified: For grids with fine wall-tangential resolution, the grid-dependent switch between RANS and LES mode may encroach inside the boundary layer resulting in a depletion of the modelled stresses and subsequent strong under-prediction of the skin friction. In strong cases this may cause a spurious prediction of flow separation known as grid-induced separation¹⁷. This problem has been successfully addressed by a range of shield functions developed to detect and protect the turbulent boundary layer from LES mode incursion. The first of these shield functions were model specific (for the SST¹⁷ model followed by the CEASM DES implementation⁴), and a generally-applicable shield function was published by Spalart et al.³⁶ known as “delayed DES” (DDES).
- The near-wall damping terms of some RANS models can become erroneously active in the LES-mode region of DES causing unphysical damping of the eddy viscosity to near zero levels³⁶. A method for deriving model-specific correction functions, Ψ , was published together with the DDES method described above³⁶.
- A “grey area”³⁴ of undefined modelling can exist between the RANS mode region and the fully-developed LES region, which is caused by the need to convert modelled RANS turbulence into predominantly resolved LES turbulence. The extent to which this is a problem is highly case specific, and is the reason why DES is better suited to very strongly separated flows than to flows with shallow separation. This problem is indeed inherent to any hybrid RANS-LES method, and it is the authors’ opinion that this can only be solved entirely by a method capable of generating physically viable synthetic resolved turbulence. The problem has however been shown to be significantly reduced through the additional substitution of L_{DES} in the eddy viscosity expression described above⁴³.
- Although explicitly not a valid application of DES, it is nonetheless attractive to attempt to employ the near wall RANS mode as a form of wall-modelling for LES resolution of attached boundary layers. Initial investigations of DES for such applications²² revealed a strong “kink” in the mean velocity profiles known as log-layer mismatch (LLM). This problem appears to have been solved by a recently published enhanced version known as “improved DDES” (IDDES)^{29,38}.

These enhanced DES versions have been implemented and studied by the authors, and the effectiveness of these will be presented together with the validation and application test cases in Sections 3 and 4 respectively.

2.3 Acoustic analogy

The far-field sound radiation of the turbulent flow can be calculated by extending the numerical solution for the limited turbulent domain to the far field with linearised approximations. One of the possibilities in the case of the radiation into free space is to use an integral over a surface based on an acoustic analogy. A discussion of various possibilities can be found in Morfey & Wright²¹. The most commonly used integral is

the procedure proposed by Ffowcs Williams & Hawkings⁶ (FW-H), which is based on the density as the wave variable. Problems occur with this approach when vortical structures or density inhomogeneities cross the control surface of the integration volume, which is necessarily the case on the downstream end of the computational domain of heated jets. These problems were avoided in the jet noise studies of TU Berlin by leaving the downstream end of the control volume open and accepting the resulting error in the far field. Morfey & Wright²¹ propose an extended acoustic analogy in which the local density is absent, a formulation that they show to be more tolerant to the truncation of volume sources external to the control surface. The sound emissions shown in this paper were computed with the classical FW-H approach.

2.4 Numerical scheme

The flow is computed using an in-house finite-volume based code that has been in use for around 10 years. The code solves the unsteady Navier–Stokes equations in either compressible or incompressible form (Section 2.2). The procedure is implicit and of second order accuracy in space and time⁴¹. All scalar quantities as well as the Cartesian components of tensor quantities are stored in the cell centres of arbitrarily curvilinear, semi-structured grids that can capture complex geometries and allow for local refinement. Diffusive terms are approximated with central schemes, whereas convective terms can be treated with central or upwind-biased limited schemes of higher order. A hybrid blending of both approaches for DES as formulated by Travin et al.³⁷ is used for all cases shown except for the jet flow and channel flow simulations. The formulation of the blending function is adopted directly as published, and is designed to deliver upwind differencing in areas of unidirectional flow or relatively coarse grids, whereas central differencing is used for finer grids, higher vorticity and lower strain. As such, in areas where LES is possible and desirable, low-dissipative central differencing is achieved, and more stable upwind differencing is used elsewhere.

The linearised equations are solved sequentially and the pressure is iterated to convergence using a pressure-correction scheme of the SIMPLE type that assures mass conservation as the pressure-correction equation is derived from the continuity equation¹¹. A generalised Rhie and Chow interpolation is used to avoid an odd-even decoupling of pressure, velocity and Reynolds-stress components²³. Transition to turbulence is not treated explicitly by a specialised predictive model, and is either tripped directly at user-defined locations or left to the turbulence model's inherent transition behaviour.

Numerical simulations of the sound emission of compressible flows can be disturbed by reflections from the boundaries of the computational domain. To avoid this, non-reflective boundary conditions are used. The boundary condition of Bogey and Bailly³ was implemented. In case of the jet a simplified version was used, which does not require knowledge of the origin of the sound waves⁴³. In addition, damping zones can be set-up on the upstream and downstream ends of the computational domain.

2.5 Grid requirements for turbulent flow prediction and sound wave propagation

The required grid resolution is determined by the requirements of both the DES and to model the sound propagation within and away from the turbulent flow source region up to the control surface used for the acoustic analogy.

The grid for the boundary layer region is dictated by the usual requirements for RANS models. The first point in the wall normal direction must be located at a distance appropriate for the turbulent wall boundary condition. In all simulations reported here, full resolution of the viscous sublayer has been conducted, such that the first point is located at $y^+ \leq 1$. The tangential wall spacing is limited only by the stability requirements of the numerical scheme with respect to high aspect ratio cells and the capturing of geometrical curvature and discontinuities as well as gradients in the flow field (e.g. sound waves and shocks).

For the LES mode region far away from the wall, the situation is much less clear cut. Although for wall-resolved LES, the maximum allowable grid cell sizes in all directions are formulated in wall units, no such concrete guidelines exist for separated regions. Although the underlying philosophy of LES stipulates that the cut-off wave number of the filter must lie within the inertial subrange of the turbulent energy spectrum, this is hard to establish in practice. Another suggestion by Pope²⁵ is that the resolved turbulent kinetic energy should account for at least 80% of the total. In any case, no a priori method is known to discern the necessary grid resolution. A pragmatic view on this issue is that the grid in LES mode should be as homogeneous as possible, and as fine as can be afforded computationally³⁵.

The correct modelling of the sound propagation requires low dispersion and low dissipation. Since the ELAN code of TUB is only of second order (Section 2.4), this necessitates a large number of grid points for the simulation of the propagation of the sound waves inside the turbulent flow region. Tests were performed to estimate the number of grid points required for a given propagation distance L , some results of which are shown in Figure 1. The amplitude loss is plotted as a function of Strouhal number $St = fL/U$. The parameters are the ratio of the propagation distance L over the grid size Δx , and the flux blending factor γ , whereby $\gamma = 1$ refers to the central scheme used in the LES region. It can be concluded that a correct simulation of the sound propagation of the technically important Strouhal number of at least 5 requires 200 uniform grid steps for a distance L . This condition must to be satisfied for the distance between the source position and any point on the control surface for the acoustic analogy, which for a free jet could be several nozzle diameters. If St is defined with the nozzle diameter D , we would need $L/\Delta x=600$ grid points for $L/D=3$.

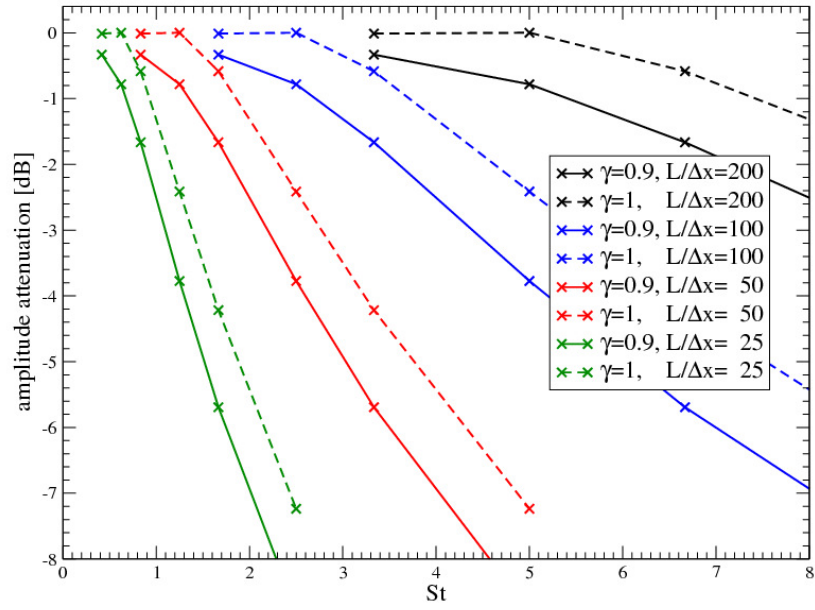


Figure 1. Decay of sound pressure amplitude due to numerical dissipation of the ELAN code as function of Strouhal number $St=fL/U$ for various spatial resolutions. $L/\Delta x$ is the number of uniform grid points per length unit L and γ is the flux blending factor.

The requirements for the temporal resolution are less severe as shown in Figure 2. A Strouhal number of $St = fD/U = 5$ would require $T_c/\Delta t = D/(U\Delta t) \cong 300$. Simulations are normally carried out with large values $T_c/\Delta t > 200$, and the error for $T_c/\Delta t \cong 200$ is rather small.

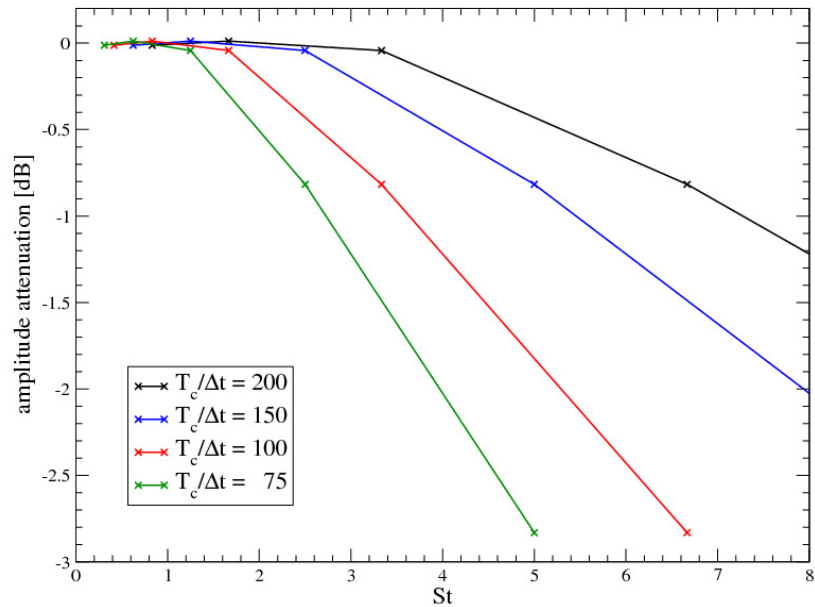


Figure 2. Decay of sound pressure amplitude due to numerical dissipation of the ELAN code as function of Strouhal number $St=fL/U$ for various temporal resolution expressed as $T_c/\Delta t$. Note the smaller range of the vertical axis in comparison to the previous figure.

2.6 Required length of time series

In order to be able to compute narrow band spectra of a stationary random signal with a filter band width Δf , the flow has to be computed with a minimum duration for a statistically stable result. A number of 50 degrees of freedom for the statistical average would require an averaging over at 25 independent time series yielding a minimum duration of $T = 25/\Delta f$, where Δf is the frequency step of the discrete Fourier transform of the signal. The jet noise computations reported below are compared with experimental data with $\Delta f = 50$ Hz, which yields duration of $T = 0.5$ s. Such a duration is very costly and was never achieved in the computations to be reported. The jet noise predictions were based on durations of $T = 0.12$ s, which are consequently statistically less stable than desirable.

An initial part of the time series may have to be discarded. A minimum guideline for this is $T_1 = L/U_c$ where L is the axial length of the computational domain in the mean flow direction and U_c is the convection velocity of the disturbances. For a jet with $L = 20D$ and $U_c = 0.6U$ we obtain $T_1 = 33D/U$ which equals $T_1 \approx 0.02$ s for the data used in the computations.

3 VALIDATION STUDIES

3.1 Correction of RANS model damping behaviour terms

To address the second problem with the original DES formulation outlined in Section 2.2, namely the erroneous activation of near-wall damping terms under certain conditions, the correction methodology proposed by Spalart et al.³⁶ has been adopted. The correction function Ψ is included in the LES length scale $L_{LES} = \Psi C_{DES} \Delta$, and the necessity and formulation of this must be defined for each model.

Such a function was found to be necessary for the SAE and SALSA models, and the functionality of the derived Ψ for the SALSA model is demonstrated in Figure 3 for the decay of isotropic turbulence. No such function is necessary for the CEASM based DES due to its two-layer formulation (Bunge et al., 2007⁴).

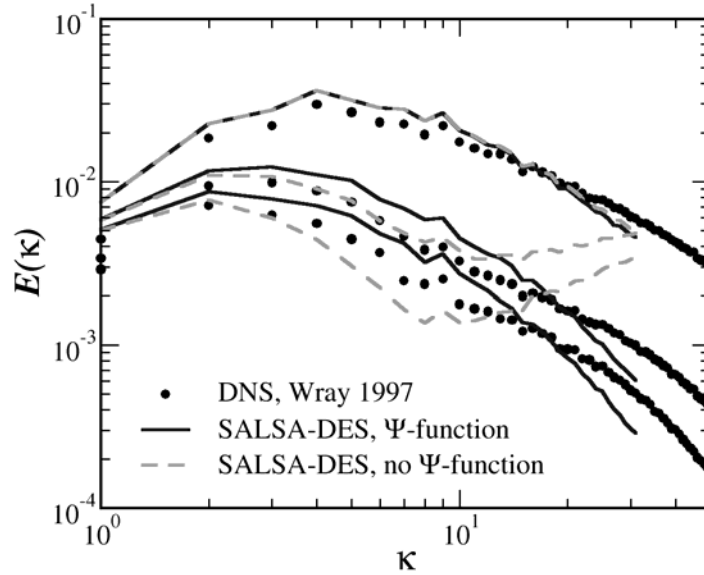


Figure 3. Decay of isotropic turbulence computed using SALSA-DES on a 64^3 grid with (solid) and without (dashed) the Ψ function compared to DNS data (Wray, 1997⁴⁰).

3.2 Modelled stress depletion and grid-induced separation

To tackle the problem of unwanted incursion of the LES mode inside the attached turbulent boundary layers, the DDES shield function has been implemented to the DES variants used, the functionality of which is demonstrated in Figure 4. For the separating-reattaching flow over a bump in a square duct at a Reynolds number of 1.04 million (based on the bump height), the shield function is seen to correctly protect the thickening boundary layers downstream of the bump.

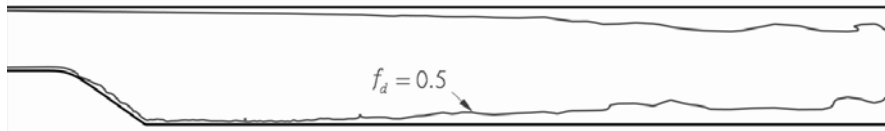


Figure 4. Mid value of the DDES shield function f_d for the flow over a bump in a square duct studied experimentally by ONERA within the DESider project (SAE-DDES).

3.3 DES as wall model for LES of attached boundary layers

Validation results will now be presented for the application of DES-based methods for wall modelling in LES (WMLES), outlined as the fourth problem in Section 2.2. The improved variant of DES known as “improved DDES” (IDDES^{38,29}) has been implemented in order to assess its effectiveness in conjunction with the ELAN solver and the SAE and CEASM turbulence models. Figure 5 shows validation results for fully-developed channel flow, where a dramatic reduction of log-layer mismatch compared to the standard DES method is demonstrated for a moderately high $Re_\tau = 4000$. The applicability to very high Reynolds numbers is shown in the right hand figure, where the SAE and CEASM implementations are compared for $Re_\tau = 18000$, with only minor differences seen in the RANS portion. From the evidence of these simulations (using the same wall-tangential grid resolution suitable for only $Re_\tau = 395$ with pure LES), wall modelled LES on the basis of DES appears to be within reach.

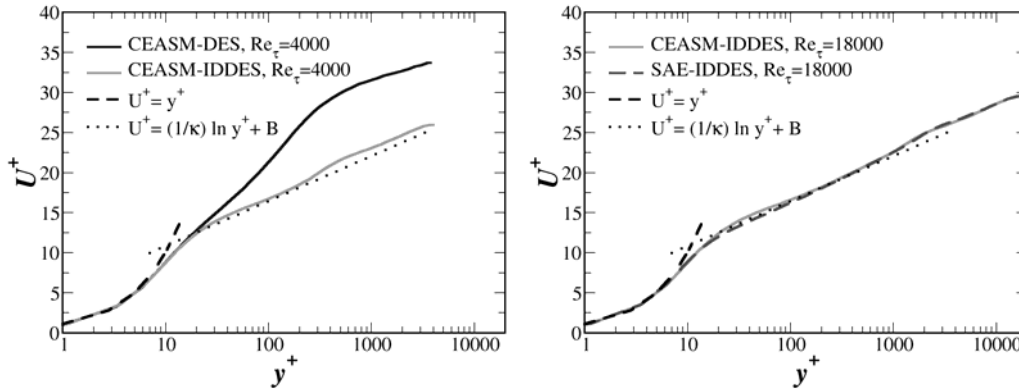


Figure 5. Comparison of IDDES with original DES formulation for fully-developed turbulent channel flow at $Re_\tau = 4000$ (*left*) and $Re_\tau = 18000$ (*right*).

That the method is generally-applicable has been shown on the basis of the ONERA bump test case, for which the appropriate DDES and wall-modelling functionality was automatically activated upstream and downstream of the flow separation, respectively¹⁹.

3.4 Validation of DES for bluff body flows with massive separation

The performance of DES for bluff body flows featuring massive separation has been validated using the flow around a circular cylinder of aspect ratio 4.8 that traverses a square channel at $Re=140000$ (based on the cylinder diameter). This configuration allows direct comparison with the highly-detailed PIV data (Perrin et al., 2006²⁴) as the entire flow domain can be directly reproduced in the simulation. To this end, a grid of some 5 million points and 96 spanwise cells has been constructed. The CEASM-based DES with the model-specific boundary layer shield function⁴ has been employed using a numerical time step corresponding to 0.03 non-dimensional units. A user-specified laminar boundary layer has been applied on the cylinder to ensure the laminar separation behaviour observed experimentally.

An impression of the flow configuration and turbulent structures resolved in the wake can be obtained from Figure 6 (*left*), where isosurfaces of the λ_2 criterion¹⁰ are plotted. An impressive level of agreement with the experiment can be seen at all levels of comparison, including the time-averaged velocity and Reynolds stress fields, velocity spectra and the phase-averaged vortex shedding motion. Numerical results for the distribution of the spanwise vorticity are compared with experimental data obtained by PIV in Figure 6 (*right*), (Mockett et al. ²⁰).

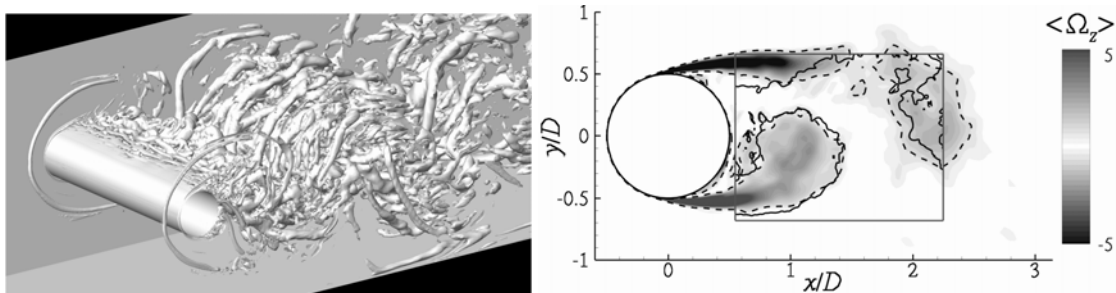


Figure 6. Resolved turbulence in the wake (isosurface of λ_2 criterion) (*left*) and phase-averaged spanwise vorticity (contour and dashed lines: DES, solid lines: PIV) (*right*).

3.5 Model sensitivity of DES

Remaining with bluff body flows, the flow around a symmetric NACA0021 airfoil in deep stall at 60° angle of attack and $Re=270000$ (based on the chord length) has been computed using DES formulated using three RANS models (SALSA, LLR and CEASM) in order to discern the level of model dependency exhibited. A very similar flow, namely around the thinner NACA0012 profile constituted one of the first published demonstrations of the DES method³⁰. The flow topology is visualised in the instantaneous snapshot of Figure 7 (*left*). A grid of roughly half a million points and a spanwise domain extent of one chord length were used, and sufficient time samples for statistical convergence were computed. No significant difference was found between the DES implementations in either the mean force coefficients or the spectra of the forces (shown in Figure 7 (*right*)). It is therefore concluded that the model dependency is very low for such massively separated flows, which arises from the dominant flow-physics being treated in LES mode. This constitutes a considerable strength of the method compared to URANS, where very strong scatter was seen between different models (Haase et al., 2006⁸; Mockett et al., 2005¹⁸) for the similar NACA0012 case.

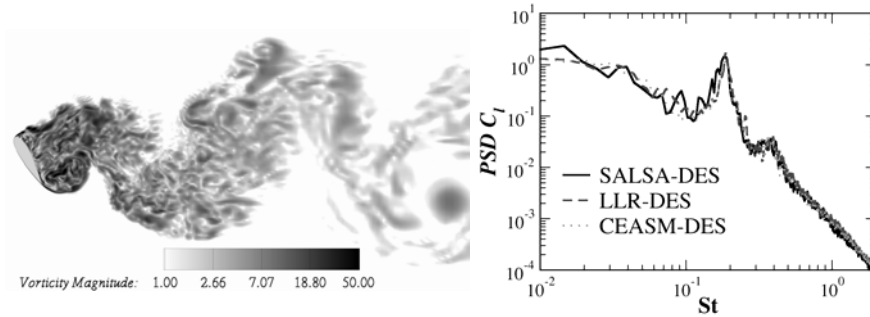


Figure 7. 2D slice of instantaneous vorticity magnitude (*left*) and comparison of lift coefficient spectra between DES implementations (*right*).

A very different story is seen for flows that exhibit more a sensitive turbulent flow separation location. An example of this is seen in the flow over the bump in a square duct introduced in Sect. 3.2, where DES was computed using two different RANS models (SAE and CEASM) on a grid consisting of around 4 million points. Strong differences are seen in the prediction of the separation points and the extent of the separated region (Figure 8), which is attributed to the fact that the separation point prediction is dominated by the RANS mode of the DES.

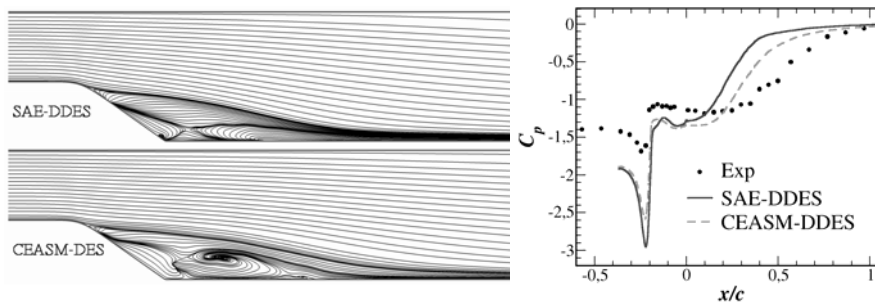


Figure 8. Bump geometry and streamlines (*left*) and pressure coefficient (referenced at the outflow) along the lower wall (*right*) compared to experiment carried out at ONERA within the DESider project.

4 NOISE PREDICTIONS

4.1 Slat noise

Beginning with the problem of airframe noise from high-lift systems, the sound generation from a deployed slat is presented. A good understanding of the underlying noise generation mechanisms is essential for the development of noise reduction strategies. Insight can be obtained from numerical simulation, which is well suited to provide detailed flow field information.

The generation of sound in the slat cove of a 3-component (slat, main element, and flap) high-lift configuration at a Reynolds number of 1.6 million based on the clean chord length has been simulated using the SALSA-DDES variant. The three-dimensional grid of some 30 million points has been simulated using 256 CPUs on the Barcelona Supercomputer Centre's "Mare Nostrum". It was found that the grid was fine enough to cause both the invasion of LES mode into the boundary layers and the erroneous activation of the near wall damping terms described in Section 3.4. The dramatic influence of the Ψ function on the eddy viscosity level can be seen from the "before and after" visualisations in Figure 9(a) and Figure 9(b), both of which were computed with the DDES shield function. Interestingly, the eddy viscosity level in the attached boundary layer is also affected; as the DDES detector depends on the eddy viscosity, the boundary layer is not correctly shielded without Ψ . An impression of the resolved turbulent structures and the generated acoustic field can be obtained from Figure 9(c).

The instantaneous wall pressures on all three elements and the unsteady flow field variables at a closed surface surrounding the whole configuration are stored in order to be able to conduct a farfield noise prediction based on the FW-H acoustic analogy when a sufficient time sample has been computed. The work is unpublished so far.

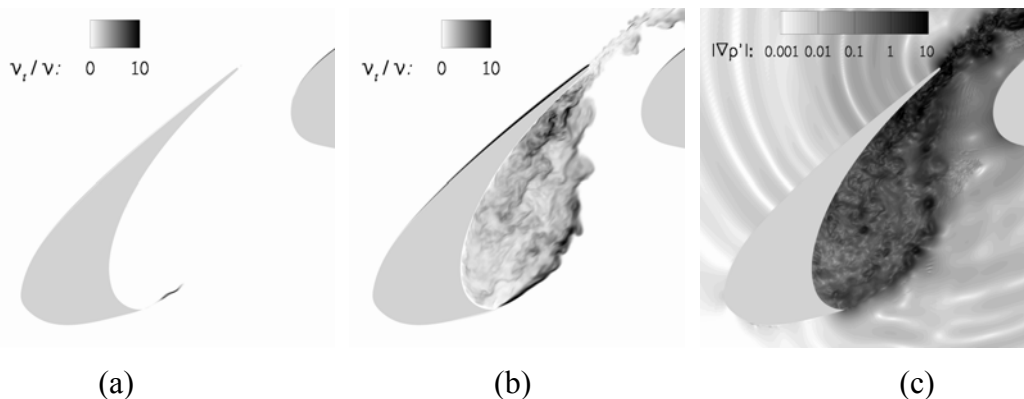


Figure 9. Eddy viscosity ratio in the slat cove region before (a) and after (b) the activation of the Ψ function. Schlieren-type visualisation of density perturbation gradients $|\nabla\rho'|$ (c).

4.2 Interaction Noise

The sound generation by an airfoil in the wake of a rod is studied within the EU PROBAND project. The numerical simulation uses a compressible CEASM DES⁴ unsteady flow field and a Ffowcs Williams & Hawkins (FW-H) acoustic analogy formulation for the far field computation. Recent studies have shown that the rod-airfoil test case is particularly suitable for the assessment of CFD codes in modelling broadband noise sources. The configuration is that of a symmetric airfoil located one chord downstream of a rod, whose wake contains both periodic and broadband vortical

fluctuations. In particular, a significant broadening of the main Strouhal peak has been observed at sub-critical vortex shedding conditions.

An experimental investigation of the rod-airfoil configuration was carried out in the high-speed subsonic anechoic wind tunnel⁹ of the Ecole Centrale de Lyon. A symmetric NACA0012 airfoil (chord $c = 0.1$ m) and a circular rod ($d/c = 0.1$) were placed in the potential core of a jet. The airfoil was located one chord-length downstream of the rod. Both bodies extended $30d$ in the spanwise direction and were supported by rigid smooth plates. The incoming velocity was 72 m/s with a turbulence intensity $Tu = 0.8\%$. The corresponding rod diameter based Reynolds number Re_d was about 48000, that of the chord length was 480000 and the Mach number M approximately 0.2.

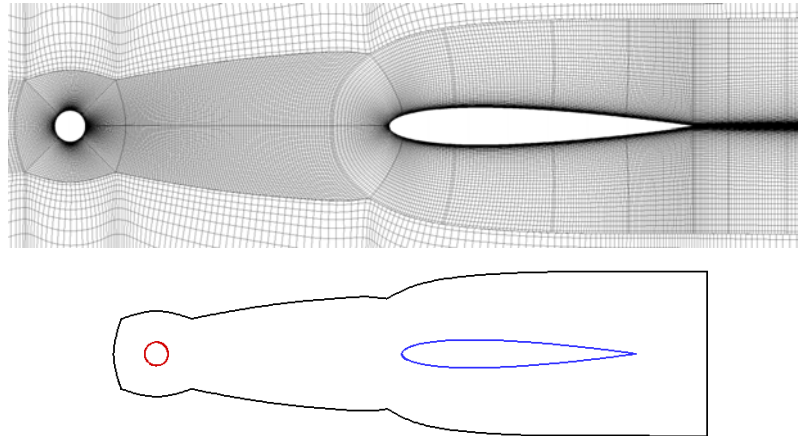


Figure 10. Grid slice (top) and integration surface for FW-H – black curve (bottom)

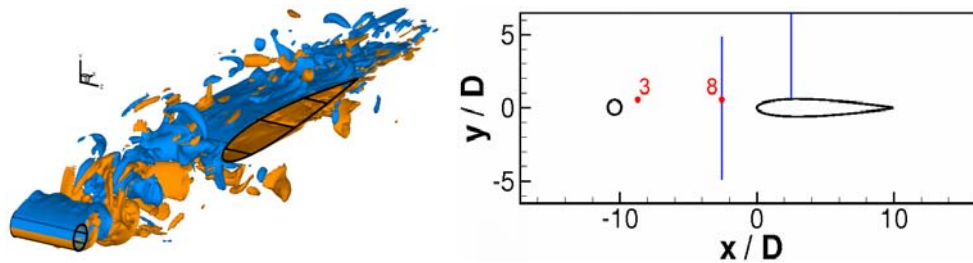


Figure 11. Instantaneous vorticity isosurfaces at $\omega_z d / u_\infty = \pm 1$ (right) and position of profiles (blue) and spectra (red) on the left

The unsteady aerodynamic field is computed using the ELAN code as described in section 2.4 and the grid filter is defined as the maximum of the grid size (Eq. 10). The computational grid extends over $180d$ in the streamwise direction, $120d$ in the cross-stream direction and $3d$ in the spanwise direction. The 2D grid shown in Figure 10 is repeated at 30 spanwise locations, with a constant spacing $\Delta z = 0.1d$. The grid is composed of about 2.3 million cells. The first cell size normal to the wall in turbulent units is $y^+ < 1.5$. The time step used in the aerodynamic simulation is 10^{-6} s. The integration surface of the FW-H is shown in Figure 10. A detailed review of the placement of the integration surface and the influence of volume sources is given by Greschner et al.⁷.

The fully three dimensional vortical flow computed with CEASM DES is shown in Figure 11. A vortex shedding pattern can be observed downstream of the rod, although strong spanwise effects prevent the formation of a regular von Kármán vortex street. The non-dimensional shedding frequency of $St = 0.183$ is close to the experimental value of 0.19.

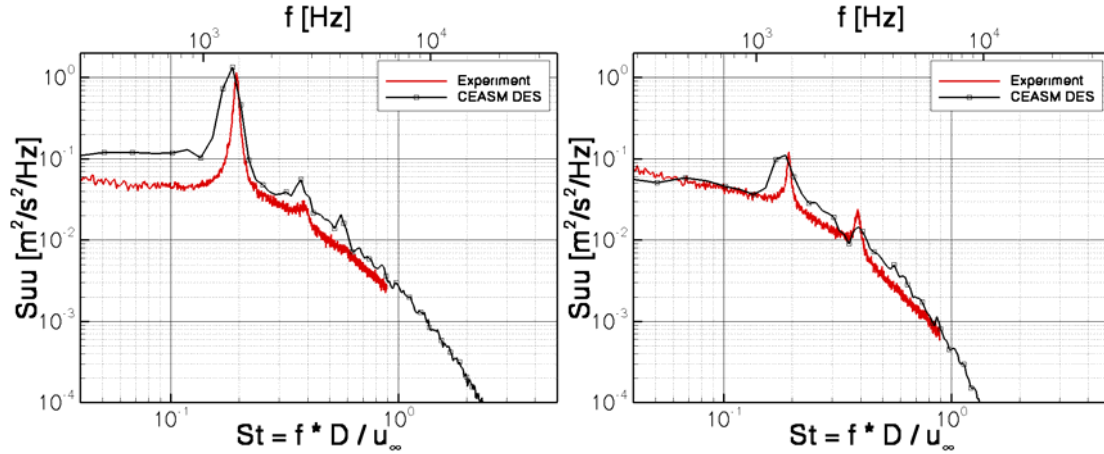


Figure 12. Velocity Spectra S_{uu} for pos. 3 and 8 compared to HWA measurements from Jacob et al.⁹.

In Figure 12, the velocity spectra S_{uu} at the two positions 3 and 8 in Figure 11 are shown. The experiment is represented by the red line and CEASM DES by the black line. The results for the simulation are based on spanwise-averaged spectra. Both figures show a peak at $St = 0.19$, which indicates that the fluctuations are mainly due to the vortex shedding. For position 3 only (located in the upper shear layer of the rod) in Figure 12 the simulation shows over-predicted levels at the very low frequency range. The slope of the spectra at higher frequencies including the levels of the second harmonic are identical with the experiment.

The far-field noise is calculated with FW-H method based on the unsteady CEASM DES data. The observers are located $185d$ from the airfoil midpoint and to the airfoil chord in the mid-span plane. The results for 45° and 90° are depicted in Figure 13. Whereas the experimental data was obtained with a spectral resolution of 4 Hz with 200 averages, the analysis of the simulated time series leads to a spectral resolution of 61 Hz with 6 averages for DES/FW-H. All results are expressed in terms of Power Spectral Density (PSD). The simulated span of three diameters ($L_S = 3d$) is less than the span of the test configuration ($L_{exp} = 30d$), therefore a scaling correction has been applied, as suggested by Kato¹².

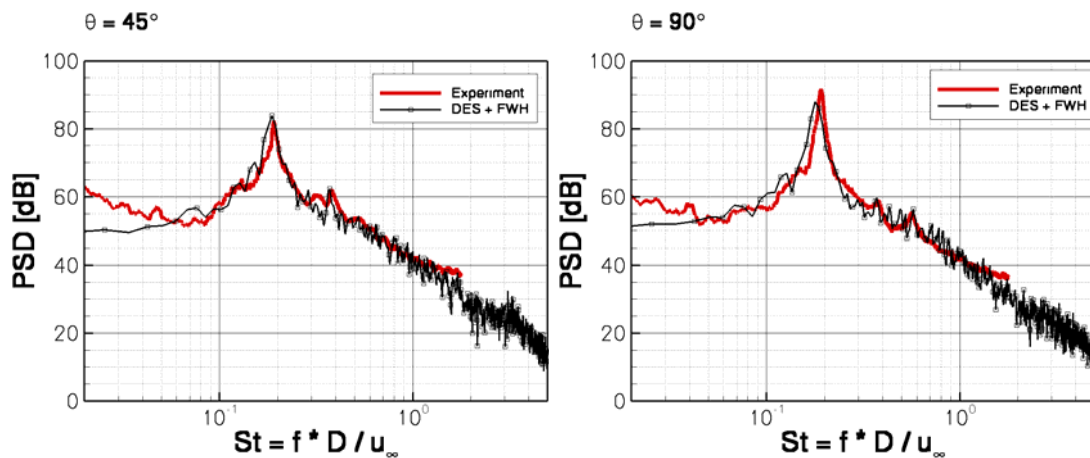


Figure 13. Far field acoustic PSD for two emission angles 45° and 90° relative to the flow direction compared to measurements from Jacob et al.⁹ ($R = 1.85$ m).

This results in a level correction of $\Delta PSD \approx 16.5$ dB around the Strouhal peak and $\Delta PSD = 10$ dB in the rest of the spectra. The DES predicts the peak of the shedding

frequency accurately. Its frequency is slightly too small, and the magnitude is under-predicted by 1 to 5 dB for the different observer positions. The OASPL for an observer normal to the flow (90°) is within 1 dB to the experiment and the computation reasonably resolves frequencies up to $St = 10$. The whole broadband spectra of the DES/FW-H shows an excellent agreement with the experiment. More information can be found in reference ⁷.

The overall performance of the presented hybrid CEASM DES/FW-H has proven to be highly satisfactory in the prediction of broadband noise spectrum generated by a complex flow configuration. The DES offers a realistic flow picture as shown by flow statistics and spectral analysis of velocity. The results of CEASM DES/FW-H method clearly show the capabilities of simulating the broadband noise sources with advanced hybrid RANS/LES approaches.

4.3 Jet noise

DES has been applied to a number of industrially-relevant coaxial jets at high Reynolds number. Of these, so far the most informative has been the short-cowl nozzle from the European research project CoJeN, as extensive experimental validation data are available inside the flow field. These consist of PIV, LDV, mean flow values, fluctuations and correlations as well as pressure fluctuation data in the near field outside the jet (but inside the computational domain) and far-field sound pressure values.

To study the effect of serrations on the near field pressure fluctuations and the far field sound, a baseline and a serrated nozzle were examined and compared. While the DES delivered the unsteady flow field in the near field, the integral based on the FW-H acoustic analogy was solved for the far field noise prediction, from which first results have been reported by Yan et al.⁴³. The geometry of the baseline nozzle is shown in Figure 14, the serrated nozzle in Figure 15.

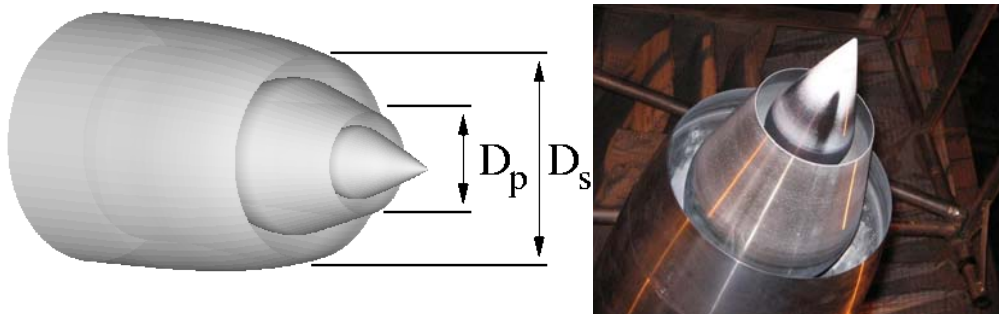


Figure 14. Geometry of the baseline version of the short cowl nozzle studied in the European research project CoJeN.

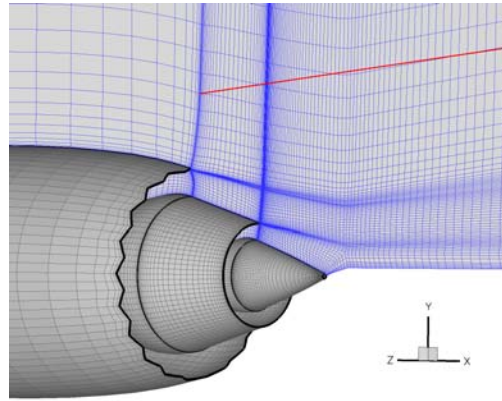


Figure 15. Geometry of the serrated nozzle studied in the European research project CoJeN and grid (every second grid point) for the simulations.

The core stream is heated and flows at $M=0.90$, whereas the bypass stream is at ambient temperature and $M=0.86$, flowing into static surrounding air.

The effect of serrations on the flow field is shown in Figure 16 based on the density isosurface. While the baseline nozzle shows ring-like vortices in the initial shear layer, the serrations force the development of three-dimensional turbulence much earlier. The number of azimuthal grid points had to be increased from 60 for the baseline case to 160 to achieve eight points per serration. The computational grid extends axially to $50 D_s$ and radially to $10 D_s$. The grid size was 3.8 million cells for the baseline case and 11 million cells for the serrated nozzle.

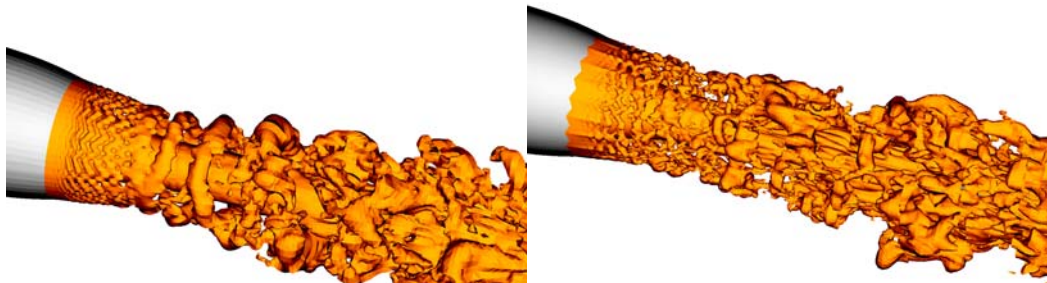


Figure 16. Comparison between flow field structures of baseline (left) and serrated (right) nozzle.

The general performance of the computation was satisfying when compared with measurements. The error in the overall sound pressure level in the far field was less than 3 dB for both the serrated and baseline cases as shown in Figure 17, while the reduction of the sound pressure level by the serration is captured excellently.

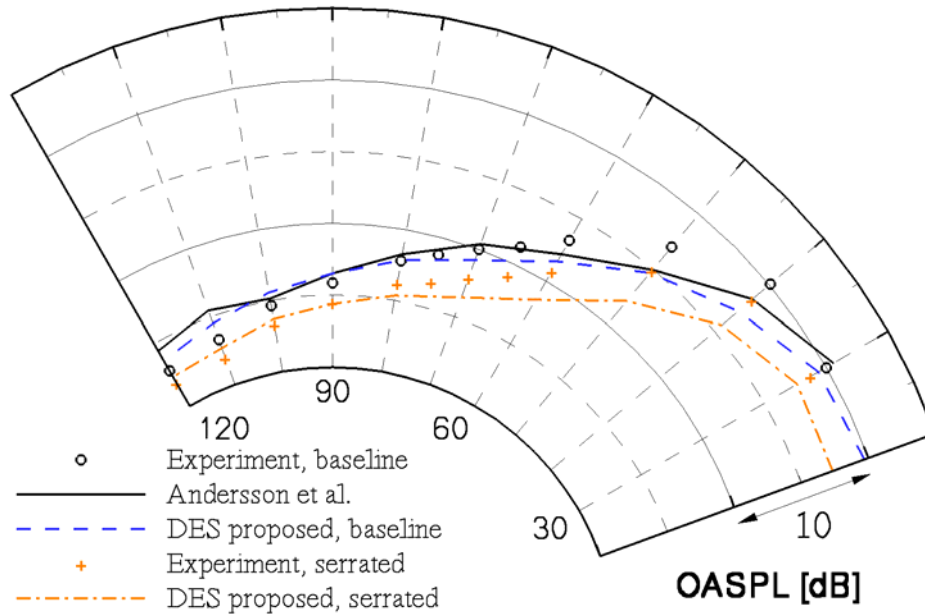


Figure 17. Far-field radiation of the coaxial jet with baseline nozzle and with serrations. Comparison of experimental data with predictions. The reduced sound pressure level of the nozzle with serrations is well predicted by the DES

The grey area problem discussed in Section 2.2 was found to have a large influence on the development of the initial free shear layer. Two Wilcox $k-\omega$ DES variants were formulated using different length scale substitution types. For the computation using the standard DES formulation, the convection of eddy viscosity from the boundary layers into the shear layer is seen to strongly damp the development of resolved turbulent structures (Figure 18 (*left*)). However, with the additional length scale substitution in the eddy viscosity expression according to Equation (13), the eddy viscosity is more strongly damped, resulting in a correspondingly enhanced development of resolved turbulence (Figure 18 (*right*)). The additional length scale substitution is therefore considered to represent a viable means of reducing the grey area problem. The length scale was computed with the cubic root for the grid sizes as grid filter length scale Δ according to Equation (11).

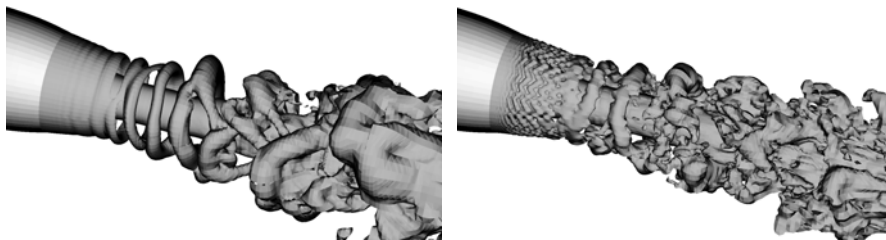


Figure 18. Density isosurfaces showing resolved structures in the jet shear layer using Wilcox $k-\omega$ DES with the standard length scale substitution (*left*) and with an additional substitution Eq. (13) (*right*).

The extent of the RANS and LES regions can be studied with the aid of Figure 19. The influence of the grid size on the border between the regions can be seen near the x -positions of the two nozzles, where the LES region extends to large radial positions. The influence on the model type in the outer region is negligible because the turbulent stresses vanish in both models.

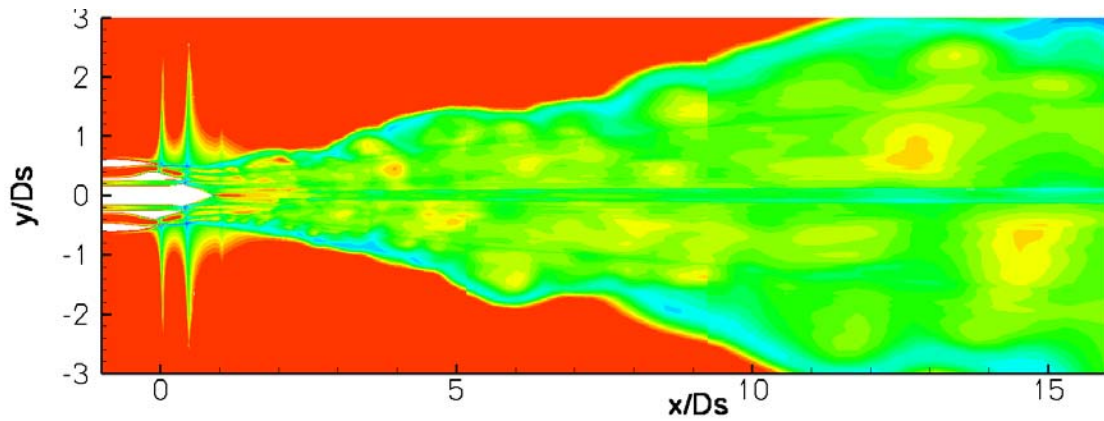


Figure 19. RANS region (red) and LES region. DES results with $\Delta=(\Delta_1 \Delta_2 \Delta_3)^{1/3}$ and L_{DES} substituted in the k -equation and μ_t expression.

Comparisons between the mean velocity profiles from the simulations and experiment are shown in Figure 20 for $x/D_s=3$. It can be seen that the mean velocity has decayed to smaller values in the simulations. However, the use of the modified μ_t equation preserves the wake of the centre body of the nozzle.

The comparison of the RMS velocity fluctuations in Figure 21 shows that the modified μ_t equation substantially reduces the velocity fluctuations to almost the experimentally determined levels. Only the fluctuations inside the wake on the centre line are over-predicted.

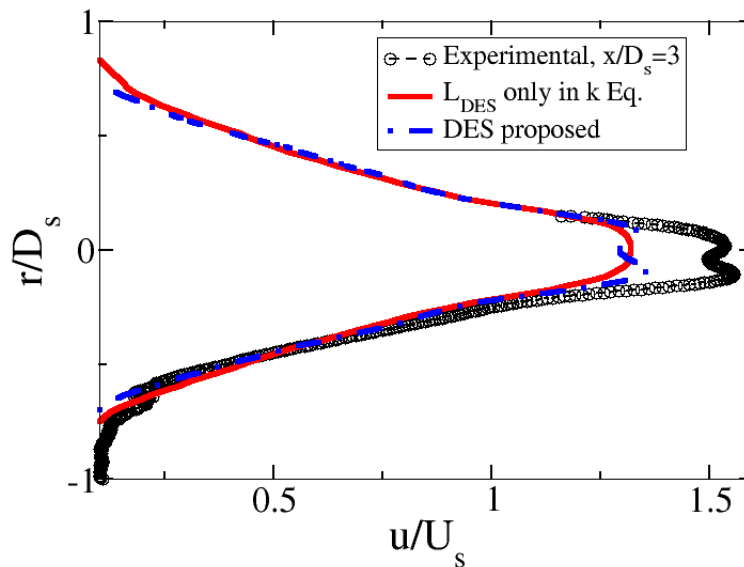


Figure 20. Mean velocity profile at $x/D = 3$ in comparison with experimental data. The modified μ_t shows an improved shape of the velocity profile, albeit still with under-predicted magnitude.

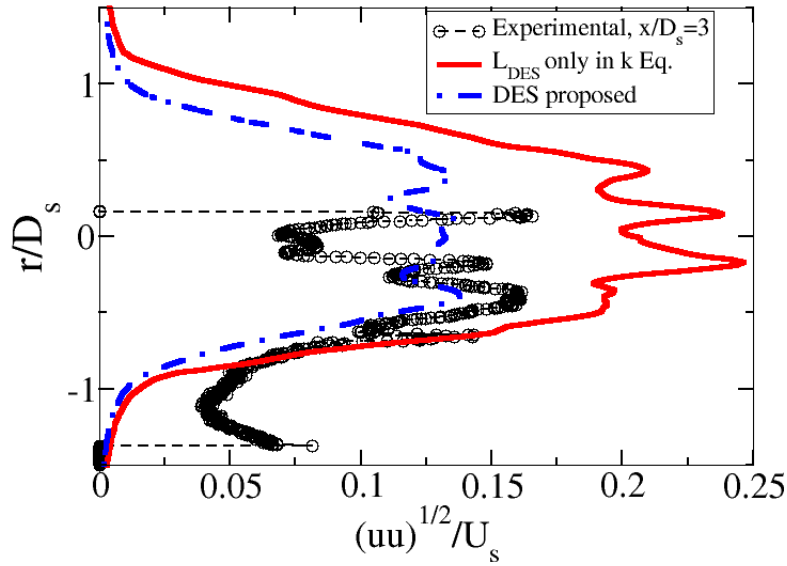


Figure 21. RMS velocity fluctuations at $x/D = 3$ in comparison with experimental data. The modified μ_t shows a substantially improved agreement of the shape of the radial fluctuation profile with experimental data.

The pressure near field just outside of the jet was measured with a line array of microphones shown in Figure 22. The microphone positions are also indicated in Figure 15. The measured rms-values are compared with the results of the simulation in Figure 23. It is obvious that the pressure fluctuations are predicted with values that are too low in the vicinity of the nozzle, which indicates that the shear layer instability is amplified too slowly. The difference between the baseline and serrated nozzle is well predicted. One cause of the slow amplifications could be that the fluctuations of the URANS solution for the nozzle boundary layer are too low. This is part of the grey area problem during the transition from RANS to LES. One other cause could be that the grid resolution in the azimuthal direction is too coarse in the vicinity of the nozzle.

Microphones in line array

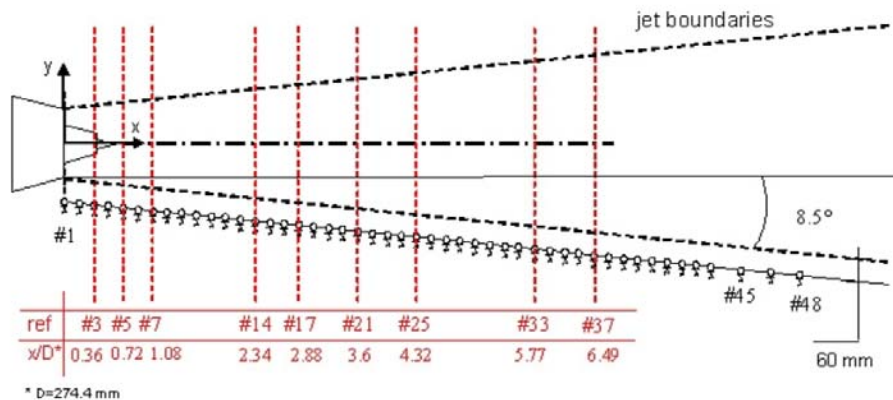


Figure 22. Near field line array of microphones for validation data.

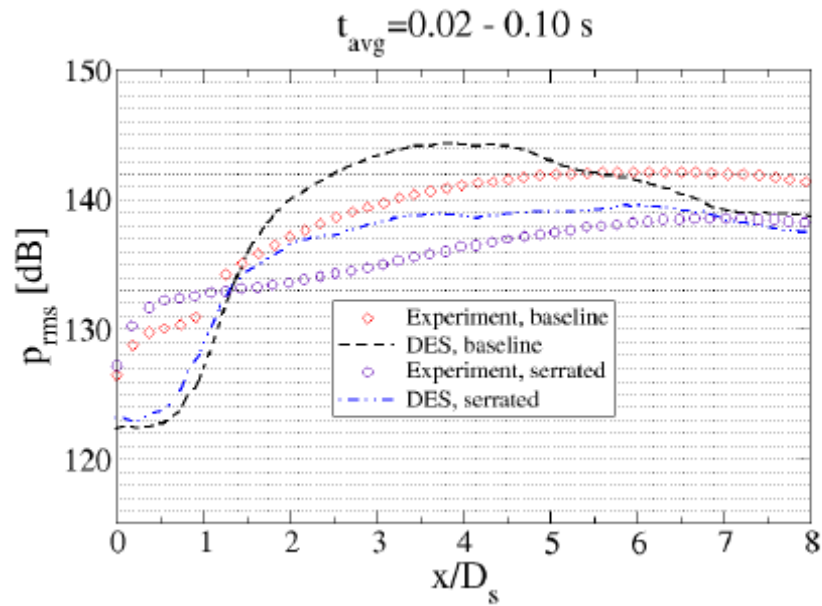


Figure 23. RMS pressure fluctuations along the outside of the jet. Results averaged over a duration of 0.08 s. The location of the line array of microphones is shown in Figure 15.

The far-field noise was computed with the FW-H integral for two different control surfaces shown in Figure 24. The space between the two surfaces is filled with relatively large grid cells. The influence of the control surface on the sound pressure spectra in the far field is shown in Figure 25 for an emission angle of 30° relative to the jet axis and in Figure 26 for an angle of 60° . The spectra based on the simulations show a rapid fall-off for frequencies above 3 to 4 kHz, which is likely caused by insufficient grid resolution according to section 2.5. This would also explain the different results for the two control surfaces, because the grid size between the two surfaces is already rather large. The cut-off frequency corresponds to a Strouhal number of $St = fD/U$ of about 2. It can be concluded that the grid must be refined over large areas by about a factor of 2.5 to achieve a frequency resolution up to $St=5$.

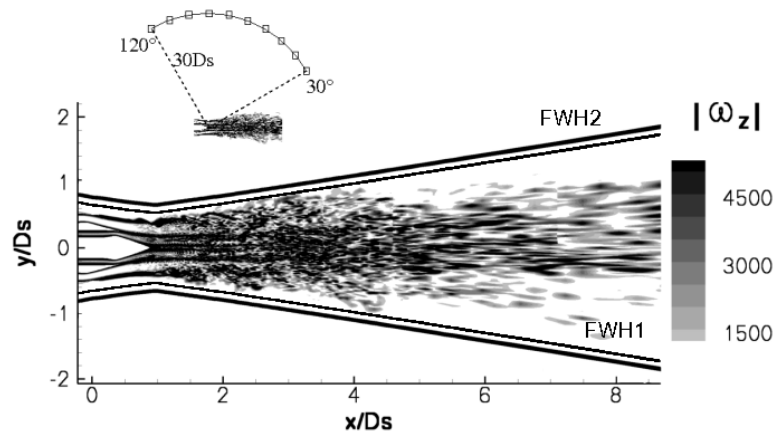


Figure 24. Definition of two FW-H Integration surfaces.

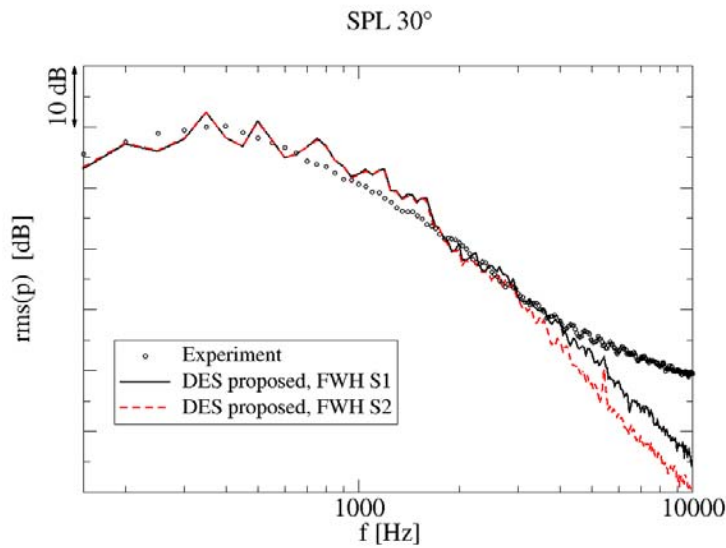


Figure 25. Frequency spectra for two FW-H integration surfaces for an emission angle of 30 degrees relative to the jet axis. The surface further away from the sources has lower spectral levels at higher frequencies.

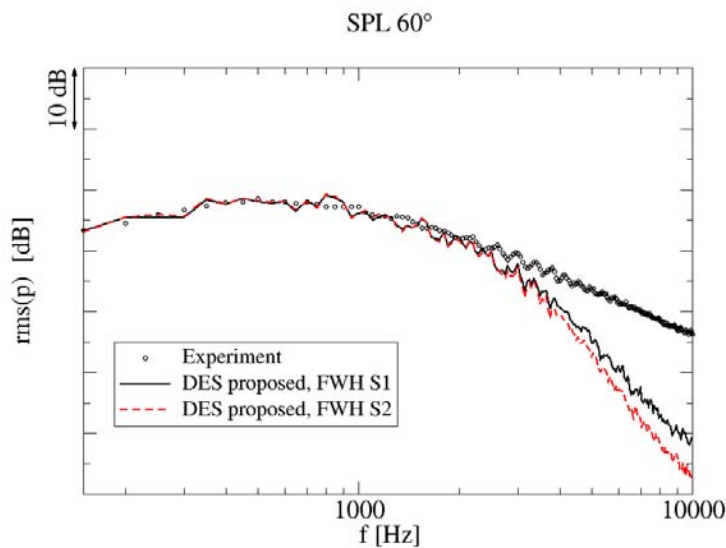


Figure 26. Frequency spectra for two FW-H integration surfaces for an emission angle of 60 degrees relative to the jet axis. The surface further away from the sources has lower spectral levels at higher frequencies.

A similar computation was performed in the German national project FREQUENZ for a coaxial jet with a long cowl nozzle, where both streams are accelerated in a common nozzle as shown in Figure 27. Two serration angles were simulated and the results were reported by Yan et al.⁴⁴. The far-field data shown in Figure 28 demonstrate an almost perfect agreement of the predictions with the measured overall sound pressure levels. The predictions with the serrations (version 2) show reduced noise levels. The fall-off (not shown here) starts at lower frequencies than in the CoJeN case which might be related to the substantially larger control surface chosen for the FW-H integral.

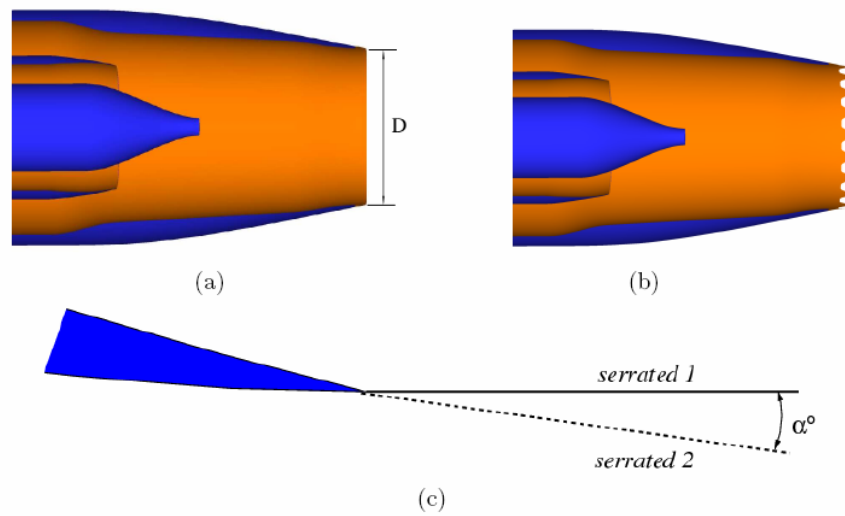


Figure 27. Geometry of the short cowl nozzle. (a) baseline, (b) serrated, (c) serration alternatives (not to scale).

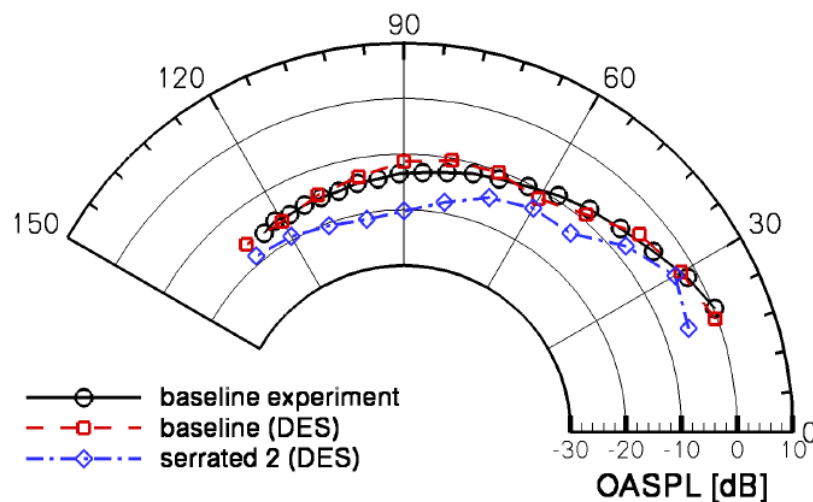


Figure 28. Predicted overall sound pressure levels in the far field for the long-cowl nozzle with and without serrations in comparison to measurements for the baseline case.

4.4 Boundary layer and trailing edge airfoil noise using wall-modelled LES

The IDDES method based on the CEASM model (near wall RANS, outer boundary layer with LES) has been applied to a simulation of boundary layer and trailing edge noise generation for a cambered NACA5510 airfoil at 7° angle of attack within the European PROBAND research project. The relatively high Reynolds number of 0.96 million (based on the chord length) is computed on a grid of 5.3 million cells. The initial field is taken from a precursor steady RANS calculation overlaid with fluctuations in the boundary layer region taken from isotropic turbulence. Figure 29 shows a slice through the computational grid and the instantaneous field. As the simulation is at a relatively early stage, some of the initial disturbances have still to dissipate. Nonetheless, the method is seen to sustain the fluctuations, suggesting that

IDDES might offer an important means of resolving boundary layer structures at high Reynolds number, which would be of considerable benefit in such aero-acoustic studies.

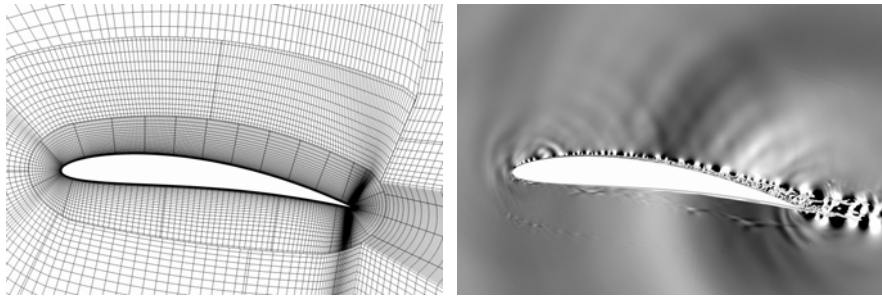


Figure 29. Spanwise slice of grid (every 2nd cell depicted) (*left*), vorticity magnitude (light contours near airfoil) and the acoustic perturbation field $\partial p/\partial t$ (far field contours) (*right*).

5 CONCLUSIONS

DES was shown to be a capable tool for the prediction of far-field noise in the cases of interaction noise (rod-airfoil) and jet mixing noise. The prediction of slat noise and trailing edge noise is well progressed. The simulation of the influence of serrations (chevrons) on the noise radiation of a jet is shown to be possible with DES. One particular advantage of DES in comparison to LES is that no unsteady forcing is required. Acoustic disturbances are introduced into the boundary layers from downstream.

Although the widespread application of DES is probably in part due to the relative simplicity of the original formulation, later studies revealed a number of shortcomings that have been successfully addressed by a number of modifications and extensions. Although these naturally increase the complexity of the DES implementation somewhat, they do serve to further enhance the robustness of the method and the range of cases for which it is applicable. As such, the DES method has reached a certain level of maturity, which should only increase its attractiveness for practical application.

The implementation and validation of these advanced DES features in an in-house university code has been presented, underlining the generality of these. The application to challenging complex test cases has served to emphasise the importance of these considerations (the derivation of appropriate Ψ functions where necessary, the implementation of shielding functions to prevent modelled stress depletion) as well as shedding light on a possible means to alleviate the grey area problem. Although still in progress, the computation of boundary layer noise using a wall-modelled LES gives promising evidence of an extended application area for DES-based methods.

The simulation of the overall sound pressure level of the far-field noise radiation was extremely successful. The predictions are within 3 dB of the experimental data. The noise reducing influence of serrations on the nozzle was correctly predicted.

Defining the grid is one of the remaining problems of the method. The grid spacing must be fine enough in the shear layers to resolve the small scales in the LES mode. In addition, the grid spacing must be small enough to properly model the sound propagation inside the flow region up to the integration surface. For technically relevant Reynolds numbers the grid size is governed by the acoustic propagation requirements.

The grid spacing in the presented cases was too coarse to enable a prediction of the sound radiation at the higher frequencies, which are important for aircraft noise.

Therefore, it is highly desirable to develop a code with higher order accuracy to reduce the number of required grid points per wave length.

6 ACKNOWLEDGEMENTS

The authors gratefully acknowledge the support of the European Community within the following 6th Framework Program projects: DESider (detached-eddy simulation for industrial aerodynamics), CoJeN (computation of coaxial jet noise), and PROBAND (improvement of fan broadband noise prediction). The support of the German Federal Ministry of Economics and Technology in the project FREQUENZ is appreciated. The computer resources, technical expertise and assistance provided on the Mare Nostrum by the BSC (Barcelona Supercomputing Center), on the IBM pSeries 690 by the HLRN (Norddeutscher Verbund für Hoch- und Höchstleistungsrechnen) and on the SGI Altix 4700 of the HLRB (Höchstleistungsrechner in Bayern) are acknowledged with thanks. The many fruitful discussions with M. Shur and M. Strelets concerning DES are very much appreciated.

7 REFERENCES

1. Andersson, N., Eriksson, L.-E. and Davidsson, L. Large-eddy simulation of subsonic turbulent jets and their radiated sound. *AIAA Journal*, **43** (2005) 1899-1912.
2. Andersson, N., Eriksson, L.-E. and Davidsson, L. LES Prediction of flow and acoustic field of a coaxial jet. *AIAA Paper 2005-2884*, 11th AIAA Aeroacoustics Conference, Monterey, California, 23-25 May 2005.
3. Bogey, S., Baily, C., and Juvé, D., "Noise investigation of a high subsonic jet using a compressible large eddy simulation," *Theoret. Comput. Fluid Mech.* **16** (2007) 273-297.
4. Bunge, U., Mockett, C. and Thiele, F. Guidelines for implementing detached-eddy simulation using different models. *Aerosp. Sc. & Tech.*, **11** (2007) 376-385.
5. Edwards, J. and Chandra, S. Comparison of eddy viscosity-transport turbulence models for three-dimensional, shock-separated flowfields. *AIAA J.*, **34** (1996) 756-763.
6. Ffowcs Williams, J.E.W. & Hawkings, D.L. Sound generation by turbulence and surfaces in arbitrary motion. *Phil. Trans. R. Soc. A* **264** (1969) 321-342.
7. Greschner, B., Thiele, F., Casalino, D. and Jacob, M.C.: Prediction of sound generated by a rod-airfoil configuration using EASM DES and the generalised Lighthill/FW-H analogy, *Computer and Fluids*, For publication.
8. Haase, W., Aupoix, B., Bunge, U. Schwamborn, D., editors *FLOMANIA - A European initiative on flow physics modelling*, vol. 94 of *Notes on Numerical Fluid Mechanics and Multidisciplinary Design*. Springer Verlag, 2006.

9. Jacob, M.C., Boudet, J., Casalino, D. and Michard, M.: A rod-airfoil experiment as benchmark for broadband noise modeling, *Theor. Comp. Fluid Dynamics*, **19** (2005) 171-196.
10. Jeong, J. and Hussain, F.: On the identification of a vortex. *Journal of Fluid Mech.*, **285** (1995) 69-94.
11. Karki, K.C. and Patankar, S.V. Pressure based calculation procedure for viscous flows at all speeds, *AIAA Journal* **27** (1989) 1167-1174.
12. Kato, C., Iida, A., Takano, Y., Fujita, H., and Ikegawa, M.: Numerical prediction of aerodynamic noise radiated from low Mach turbulent wake, *AIAA Paper 1993-0145*, 31st Aerospace Sciences Meeting and Exhibit, (1993).
13. Li, X. D. Schemel, C., Michel, U. and Thiele, F. "On the azimuthal mode propagation in axisymmetric flow ducts." *AIAA Journal* **42**, 2019-2027, 2004.
14. Li, X. D. Schönwald, N., Yan, J and Thiele, F. "Numerical study of the acoustic radiation from a scarfed inlet." *AIAA Paper 2003-3245*. 9th AIAA/CEAS Aeroacoustic Conference Hilton Head, 12-14 May 2003
15. Li, X. D. Richter C. and Thiele, F. "Extension of time-domain impedance boundary conditions for subsonic mean flows." *Journal of Acoustical Society of America*, **119** (2006) 2665-2676.
16. Lübcke, H., Rung, T. and Thiele, F. Prediction of the spreading mechanisms of 3D turbulent wall jets with explicit Reynolds-stress closures. In *Eng. Turb. Mod. & Exp.* **5** (2002) 127–145.
17. Menter, F. and Kuntz, M. (2004): Adaption of eddy-viscosity turbulence models to unsteady separated flow behind vehicles. In *Lecture notes in applied and computational mechanics vol. 19*. Springer Verlag.
18. Mockett, C., Bunge, U. and Thiele, F. Turbulence modelling in application to the vortex shedding of stalled airfoils. In *Eng. Turb. Mod. & Exp.* **6** (2004) 617–626.
19. Mockett, C.; Greschner, B.; Knacke, T.; Perrin, R.; Yan, R.; Thiele, F.: "Demonstration of improved DES methods for generic and industrial applications." In: *Proceedings of the 2nd Symposium on Hybrid RANS-LES methods*, Corfu, Greece, 2007.
20. Mockett, C., Perrin, R., Reimann, T., Braza, M. and Thiele, F. (2007): Analysis of detached-eddy simulation for the flow around a circular cylinder with reference to PIV data. In *Proc. IUTAM Symp. Unsteady Separated Flows and their Control*, Corfu, Greece.
21. Morfey, C.L. and Wright, M.C.M.: Extensions of Lighthill's acoustic analogy with application to computational aeroacoustics. *Proc. R. Soc. A* **463** (2007) 2101-2127.
22. Nikitin, N., Nicoud, F., Wasistho, B., Squires, K. and Spalart, P. An approach to wall modeling in large-eddy simulations. *Phys. of Fluids*, **12** (2000) 1629–1632.
23. Obi, S., Perić, M. and Scheurer, M. Second moment calculation procedure for turbulent flows with collocated variable arrangement, *AIAA Journal* **29**, 585-590, 1991.
24. Perrin, R., Braza, M., Cid, E., Cazin, S., Barthet, A., Sevrain, A., Mockett, C., and Thiele, F. (2006): Phase averaged turbulence properties in the near wake of a

- circular cylinder at high Reynolds number using POD. In Proc. 13th Int. Symp. Applications of Laser Techniques to Fluid Mechanics, Lisbon, Portugal.
25. Pope, S.P.: Turbulence, Cambridge University Press, 2000
 26. Richter, C. Thiele, F. Li X. D. and Zhuang, M. "Comparison of Time—Domain Impedance Boundary Conditions by Lined Duct Flows." AIAA Journal, to be published 2007.
 27. Rung, T. and Thiele, F. (1996): Computational modelling of complex boundary-layer flows. In Proc. 9th Int. Symp. Transport Phenomena in Thermal-Fluid Engineering, Singapore.
 28. Rung, T., Bunge, U., Schatz, M. and Thiele, F. Restatement of the Spalart—Allmaras eddy-viscosity model in strain-adaptive formulation. AIAA J., **41**, 1396–1399, 2003.
 29. Shur, M., Spalart, P., Strelets, M. and Travin, A. (2007) A hybrid RANS-LES model with delayed DES and wall-modelled LES capabilities. International Journal of Heat and Mass Transfer. To be published.
 30. Shur, M., Spalart, P.R., Strelets, M. and Travin A. Detached eddy simulation of an airfoil at high angle of attack. Engineering Turbulence Modelling and Experiments **4** (1999) 669-678.
 31. Shur, M., Spalart, P.R., Strelets, M. and Travin A.K. Towards the prediction of noise from jet engines. Int. J. of Heat and Fluid Flow, **24** (2003) 551-561.
 32. Shur, M.L., Spalart, P.R., Strelets, M.Kh. and Garbaruk, A.V. Further steps in LES-based noise prediction for complex jets. AIAA Paper 2006-0485. 44th AIAA Aerospace Science Meeting, 9-12 January 2006, Reno, Nevada.
 33. Spalart, P. and Allmaras, S. (1992): A one-equation turbulence model for aerodynamic flows. In Proc. 30th AIAA Aerospace Sciences Meeting and Exhibit, Reno, Nevada, USA, 1992.
 34. Spalart, P., Jou, W., Strelets, M. and Allmaras, S. Comments on the feasibility of LES for wings, and on a hybrid RANS/LES approach. 1st ASOSR Conference on DNS/LES, 1997.
 35. Spalart, P. R. (2001): Young person's guide to detached eddy simulation grids. NASA/CR-2001-211032, 2001.
 36. Spalart PR, Deck S, Shur M, Squires K, Strelets M, Travin A. "A new version of detached-eddy simulation, resistant to ambiguous grid densities." Theor. Comp. Fluid Dynamics, **20**, 181-195, 2006.
 37. Travin, A., Shur, M., Strelets, M., and Spalart, P. (2000): Physical and numerical upgrades in the detached-eddy simulation of complex turbulent flows. In Proc. 412th Euromech Coll. LES and Complex Transitional and Turbulent Flows, Munich, Germany.
 38. Travin, A., Shur, M., Spalart, P. and Strelets, M. (2006): Improvement of delayed detached-eddy simulation for LES with wall modelling. In Proc. Eur. Conf. Comp. Fl. Dyn. ECCOMAS CFD 2006, Egmond aan Zee, The Netherlands.
 39. Wilcox, D. Reassessment of the scale-determining equation for advanced turbulence models. AIAA J., **26** (1988), 1299–1310.

40. Wray, A. (1997): Unpublished DNS data. In “Test Cases for the Validation of Large-Eddy Simulations of Turbulent Flows”, <ftp://torroja.dmt.upm.es>.
41. Xue, L. (1998): Entwicklung eines effizienten parallelen Lösungsalgorithmus zur dreidimensionalen Simulation komplexer turbulenter Strömungen. PhD thesis, Technische Universität Berlin, Universitätsbibliothek (Diss.-Stelle).
42. Yan, J., Mockett, C. and Thiele, F. Investigation of alternative length scale substitutions in detached-eddy simulation. *Flow, Turb. & Comb.*, **74** (2005), 85–102.
43. Yan, J., Tawackolian, K., Michel, U. and Thiele, F. (2007): Computation of jet noise using a hybrid approach. AIAA Paper 2007-3621. 13th AIAA/CEAS Aeroacoustics Conference: Rome, Italy, May 2007
44. Yan; J. Panek; L. Thiele F.: “Simulation of jet noise from a long-cowl nozzle with serrations.” AIAA Paper 2007-3635, 13th AIAA/CEAS Aeroacoustics Conference, Rome, Italy, May: 2007.